Modal analysis of piezoelectrically actuated plates with built-in stress by computationally augmented interferometric experiments

Hamed Salmani [a], Elisabetta Bodo [b], Ulrik Hanke [a], Andreas Vogl [c], Shruti Jain [c], Sabina Merlo [b], Einar Halvorsen [a],*

[a] Department of Microsystems,Campus Vestfold, University of South-Eastern Norway, Raveien 215, 3184 Borre, Norway
[b] Department of Electrical, Computer and Biomedical Engineering, University of Pavia, Via Ferrata 5, 27100 Pavia, Italy
[c] Department of Microsystems and Nanotechnology, SINTEF Digital, Gaustadalléen 23C, 0373 Oslo, Norway

ARTICLE INFO

ABSTRACT

The conventional laser doppler vibrometers for modal analysis of micro-structures are expensive and sometimes inaccessible. In this work, a compact, fiber-based interferometric setup is used to carry out the modal analysis of initially deflected piezo-actuated micro-plates with different designs. The finite element method provides actual mode shapes visualization in the frequency range up to 100 kHz using the spectral results of vibration measurements performed at a few selected spots of the plate. This method is capable of finding the resonance frequencies and distinguishing the mode shapes. It has also allowed us to investigate the impact of bias voltage on the actual values of the resonance frequencies.

1. Introduction

Piezoelectrically actuated plates are widely used in Micro-Electro-Mechanical Systems (MEMS) such as tunable lenses [1–3], piezoelectric Micromachined Ultrasonic Transducers (pMUT) [4], and micro-pumps [5] etc. The microfabrication of a multi-layer piezoelectric plate is performed at different temperatures for each layer. Due to the thermal mismatch between different layers, the resulting built-in stress may cause buckling of the plate after fabrication, which consequently deforms the plate from its desired flat shape [6]. The built-in stress changes not only the initial shape of the structure, but also the stiffness is changed. Therefore, the dynamic behavior of the deformed plate is changed with respect to a flat plate as the resonance frequencies are shifted [7–10] and some mode shapes are superposed [11,12].

In order to find the resonance frequencies and mode shapes of a micro-plate, an optical instrument for non-contact dynamic characterization is required. Conventional Laser Doppler Vibrometers (LDVs) can be successfully applied to measure the resonance frequencies and identify the mode shapes of the structure [13–16]. Although they are convenient since they allow vibration detection by automatic scanning of the structure, they are expensive and are not easily accessible.

The dynamic response of micro-devices can be successfully characterized also with optical methods based on interferometric measurements performed in just a few well-selected spots on the structure. The simplest measurement is capturing the response of a single point to detect some of the resonance frequencies of a structure [17,18]. In spite of the simplicity of a single point measurement, it will not provide enough information to form the mode shapes. Recording the vibration spectral profile in two positions provides more data to shape some modes, but it is still not enough to extract the higher order mode shapes [19–21]. In some cases, choosing a few points might be sufficient to plot specific mode shapes, like scanning along the radial line of a circular plate to find the axisymmetric modes [22]. It is of interest to apply similar techniques in the case of plates exhibiting several vibration modes with different geometries in a relatively narrow frequency range. To achieve a good matching between mode shape and resonance frequency, a fine scan of the whole structure would be required to perform vibration measurements in a large number of spots [23–25]. However, this procedure would become laborious.

In this work, we have utilized an appropriate Finite Element (FE) model to visualize the mode shapes of piezo-actuated plates with built-in stress. This helps in identifying the most preferable positions on the structure for frequency response measurements at just a few spots. The piezoelectric plate was actuated with electrical white noise and measurements were performed at a limited number of positions within a quarter of a plate. In order to visualize the mode shapes, we have

---

* Corresponding author.
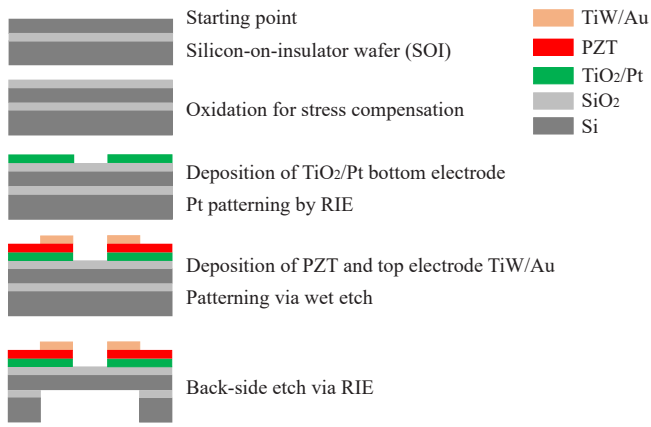*E-mail address:* Einar.Halvorsen@usn.no (E. Halvorsen).

Fig. 1. Main processing steps for fabrication.

Table 1
Electro-mechanical coupling coefficients of properties of PZT.

d_{31} (10^{-12} C/N)	d_{33} (10^{-12} C/N)	d_{15} (10^{-12} C/N)
-134	296	440

Table 2
Plate layers thicknesses.

Layer	Thickness (μm)
TiW/Au	0.25
PZT	2.00
TiO$_2$/Pt	0.15
SiO$_2$	2.00
Si	7.12

Table 3
Built-in stress for each layer of the plate.

Layer	Built-in stress (MPa)
SiO$_2$	-300 ± 30
TiO$_2$/Pt	1100 ± 100
PZT	60 ± 10

Table 4
Mechanical material properties of each layer of the plate.

Material Properties	SiO$_2$[30]	TiO$_2$/Pt[31]	PZT	Au[32]
E (Gpa)	70	170	82	80
ν	0.17	0.35	0.38	0.44
ρ (kg/m^3)	2200	21450	7500	19300
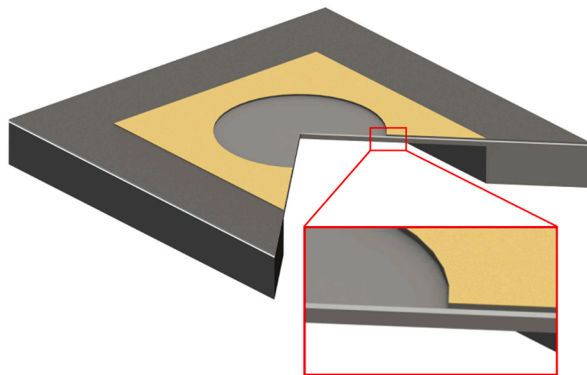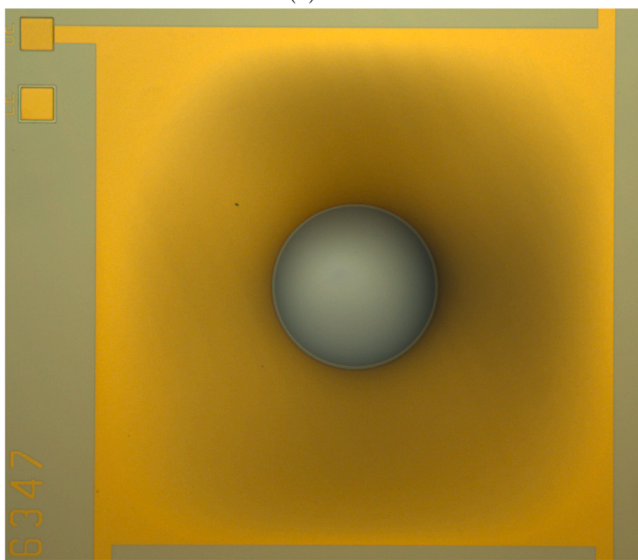
Fig. 2. Actuator layers. (a) 3D sketch of the plate. (b) Microscopic image of the fabricated plate.

compared the experimentally detected resonance frequencies with those extracted from the Finite Element Method (FEM). Then, knowledge of the resonance frequency helps to figure out an approximate mode shape using FEM. Though this technique needs more effort in post-processing than that is required when an LDV is available, preparing a FE model is anyway necessary in both cases to estimate the scanning frequency range and the measurement points.

2. Fabrication and characterization

The modal analysis is performed on piezo-actuated plates fabricated on a (100) silicon SOI wafer with the process like those reported in [26, 27]. The main processing steps used in fabrication of the plates are shown in Fig. 1. The SOI wafer consisted of a 400 μm thick silicon substrate (handle silicon), a 0.5 μm thick buried oxide layer and a 8 μm thick device layer on top of the oxide. Thermal oxidation was done to form SiO$_2$ stress compensation layer. A thin Ti layer was sputtered followed by its oxidation to form a diffusion barrier layer of 32 nm TiO$_2$. A layer of 100 nm Pt {111} is then sputtered to be used as the bottom electrode. Pt was then patterned using dry etch. A thin seed layer of Lithium Niobate (LNO) was deposited followed by deposition of 2 μm thick Chemical Solution Deposition-lead zirconate titanate (CSD-PZT) using multilayer spin coating process. LNO and PZT sol-gel solutions from Mitsubishi Materials Corporation, Japan, were used. Each layer was annealed before another layer was spin coated. The resulting PZT film has high {100} texture and excellent piezoelectric properties as mentioned in. Tab. 1. Next a thin buffer layer of TiW was sputtered followed by sputtering of 250 nm Au, which served as top electrode. All sputtering processes were done in an ENDURA, Applied Materials, sputtering tool. Two photolithographic masks were used to pattern top electrode and PZT using wet etch process. A thin layer of alumina (ca. 40 nm) was deposited at Picosun Oy (Finland), and patterned using a photo mask before depositing and patterning a TiW/Au metal pad. The back side was opened via DRIE of the handle wafer and dry etching of the buried oxide. The wafer was finally diced into 5×5 mm^2 chips as shown in Fig. 2. The thickness of each layer after the process is listed in Tab. 2.
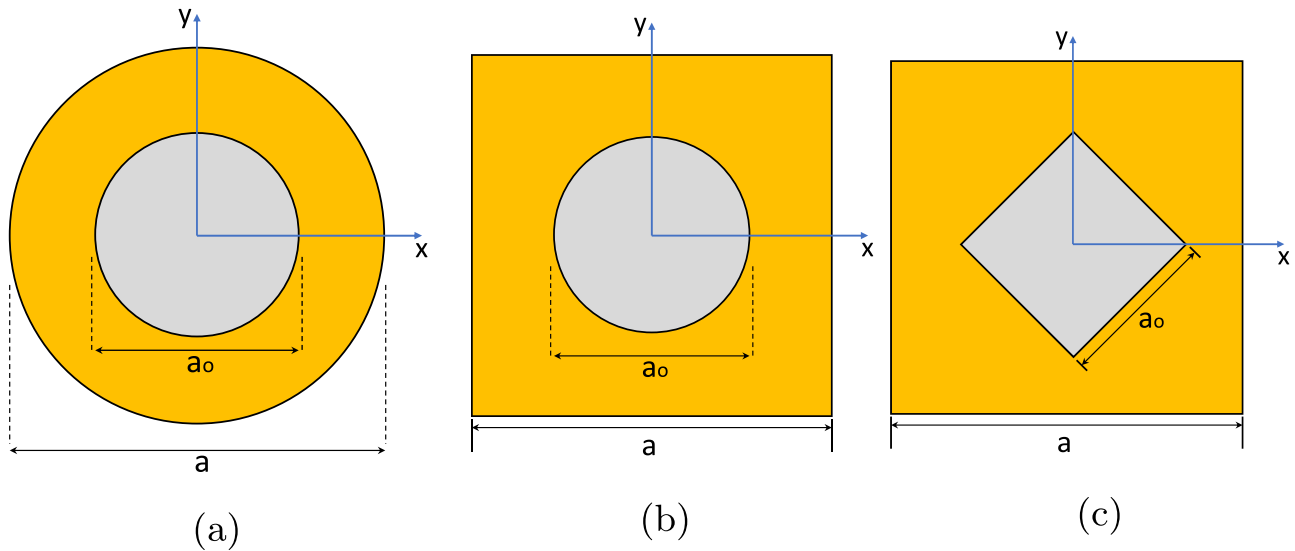
Fig. 3. Plate geometries. (a) Circular plate with circular opening (CC). (b) Square plate with circular opening (SC). (c) Square plate with square opening (SS).

Table 5
Dimensions of the plates.

Plate Geometry	$a_0 (\mu m)$	$a\ (\mu m)$
CC1	1130	3200
CC2	2100	3200
SC1	1130	3200
SC2	2100	3200
SS1	1130	3200
SS2	2100	3200

The plates are initially deformed in short-circuit condition due to the existence of built-in stress. Stress values in each layer are determined by depositing a material stack of PZT with top and bottom electrodes on a wafer. The measurements are performed on 15 samples which are diced into 8.3×8.3 mm^2 squares. Each layer was then etched. Curvature measurements were done corresponding to each layer which was converted to stress values via Stoney's equation [28] i.e. one assumes a thin stressed layer on top of a thick substrate that is deformed by the stress in the thin layer. Calculated stress values are shown in Tab. 3.

The material properties of anisotropic silicon are given in [29], and the Young's modulus (E), Poisson's ratio (ν) and density (ρ) of the plate layers are given in Tab. 4. The relative permittivity of PZT is 1200.

We investigated samples with an opening at the center, which are commonly used in a tunable lens. Although the opened areas of the samples are made up of opaque Si and SiO$_2$, they may be considered as test structures for tunable lens actuators. Experiments are conducted on three configurations including circular plate with circular opening (CC), square plate with circular opening (SC) and square plate with square opening (SS). The static actuator performances of similar configurations are modelled in [33,34]. The configurations of the plates are sketched in Fig. 3 and their dimensions are given in Tab. 5.

3. Finite element modeling

Before conducting any experiment, preparing an appropriate FE model is necessary to get insight into the static and dynamic behavior of the structures. Knowing the simulated resonance frequencies and the mode shapes of the structure is an aid when determining the appropriate experimental setup, frequency scanning range and the most descriptive measurement positions. We use COMSOL Multiphysics®[35] to model the structures and find the mode shapes. Using the geometry and material parameters of Sect. 2 and Sect. 3, all six structures are modelled in COMSOL with quadrilateral hexahedron elements. A FE analysis convergence study is also performed to ensure accuracy of the results. Because of the initial deflection as a result of built-in stress, a geometrically nonlinear static analysis must be carried out to get the initial shape. Therefore, the solution procedure consists of two steps, i.e. first finding a geometric nonlinear static solution followed by obtaining a prestressed eigenvalue solution. The static solution is attained incrementally by step-wise increasing a load factor. The load factor is multiplied by the values of the built-in stress in each layer and varies from 0 to 1 with step 0.1. When the load factor equals 0, the plate is flat in the absence of built-in stress. The final configuration of the deformed plate is calculated when the maximum values of built-in stress are applied at the load factor 1. By this incremental solution approach of the geometrically nonlinear model, the deformed geometry and stress induced stiffness matrix are calculated at the first step of the solution. At the second step of the solution, the updated geometry, stiffness and mass matrices of the model are imported as an input for the prestressed eigenfrequency solution. As a consequence, the resonance frequencies of the deformed structures will shift with respect to resonance frequencies of the the flat plate. The effects of built-in stress on the center displacement and first six resonance frequencies of the plate CC2 are plotted in Fig. 4. It is observed that the plate is softened as the result of the large compressive stress in the SiO$_2$ layer up-to a point of minimum stiffness. The behaviour is similar to buckling instability but differs in
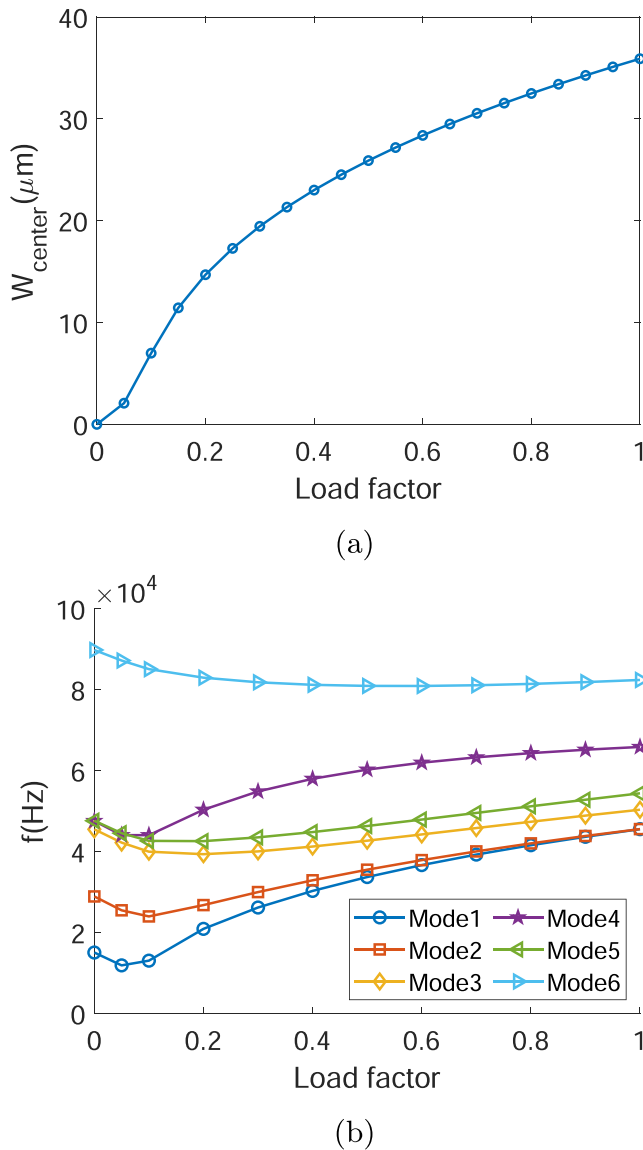
Fig. 4. Effect of the built-in stress on (a) displacement of the center point and (b) resonance frequencies of the plate CC2.

being a smooth transition with a finite minimum stiffness. The non-linear behavior of the displacement and the frequency shifts are clearly shown in Fig. 4(a) and (b) respectively. When the compressive load is dominant, the softening effect is observed whereas the structure is stiffer when the bending moment dominates.

4. Device characterization

In this section, the measurement technique and setup are described in details. Before performing any measurement, the samples are poled by 150 kV/cm electric field at 150 ˚C using an aixACCT TFA 320-E instrument. The direction of the polarization is from the bottom electrode toward the top electrode. Then, the static and dynamic measurements are performed.

4.1. Static measurement

The static measurement gives the profile of the deformed plate due to the built-in stress while the electrodes are short-circuited. For this purpose, a DEKTAK 150 Profilometer is employed to scan the profile of the plate along the x direction with scanning resolution of 300 nm.

The residual stress values of Tab. 3 are obtained within a range, while it is required to apply specified values as the load in FE modelling. There is a discrepancy between the center point displacements of the measurement and simulation when applying the maximum values of the built-in stresses without a correction factor. We fit the center displacement of the sample CC2 from FEM to the measured one by multiplying the maximum built-in stresses values with a correction factor. The correction factor is calculated as 0.8897, which results the stress values of all layers to be within the limits given in Tab. 3. Because all of the samples are taken from the same wafer, we use the same factor to model the other samples.

The results of the static measurements and their comparison with FE simulations are shown in Fig. 5. The simulated static displacements of all samples agree well with the experimental ones, which verifies the fitted values of the built-in stresses. This ensures that the FE model can be used for further modal analysis.

The results of Fig. 5 show that for plates having the same configuration, the center displacement of the plates with larger opening are higher than those with smaller opening. To reveal the reason for this, the simulated center displacements of the samples CC1 and CC2 are plotted in Fig. 6(a) as the load factor is increased. The center displacement of the sample CC2 is higher than the center displacement of the sample CC1 when the load factor equals 1. It is also observed in Fig. 6(b) that the minimum frequency occurs at a lower load factor along with a higher slope in the sample CC2. This behavior can be understood as the compressive built-in stress affecting the larger opening area with lower stiffness in sample CC2.

4.2. Dynamic measurement

The instrumental and optical configuration of the laser vibrometer applied for dynamic analyses of the piezo-actuated plate is reported in Fig. 7. It consists essentially in a fiberoptic Michelson interferometer that allows performing spatially-resolved spot optical measurements of vibration frequencies. Light from a DFB semiconductor laser (Mitsubishi ML925B11F-01), emitting at the wavelength $\lambda = 1550$ nm and operating at T = 22˚ C with 16 mA driving current (LD in Fig. 7) is launched into an input port of a 2×2, 50:50 splitting ratio, fiberoptic coupler (Thorlabs bidirectional 2×2 FO couplers with 50:50 splitting ratio and flat spectral response: TW1550R5F2) (C in Fig. 7). Light is thus directed along the "measuring arm" toward the device under test and along the "reference arm" to a reference-mirror. Impinging light is projected orthogonally onto the device under test (and the back reflected light is then similarly collected) by means of pigtail style focusers, based on 9/125 μm core-cladding diameter single-mode fibers, incorporating an aspheric lens with focal length f = 3.9 mm, with 40 dB return loss, by OzOptics, USA (LPF-04–1550–9/125-S-5–23.5–3.9AS-40–3S-3–1). The spot generated on the device has a diameter of 50 μm, thus allows performing measurements with very good spatial resolution. The interferometric signal, generated by radiation back-reflected from the mirror interfering with radiations back-reflected from the plate, is then
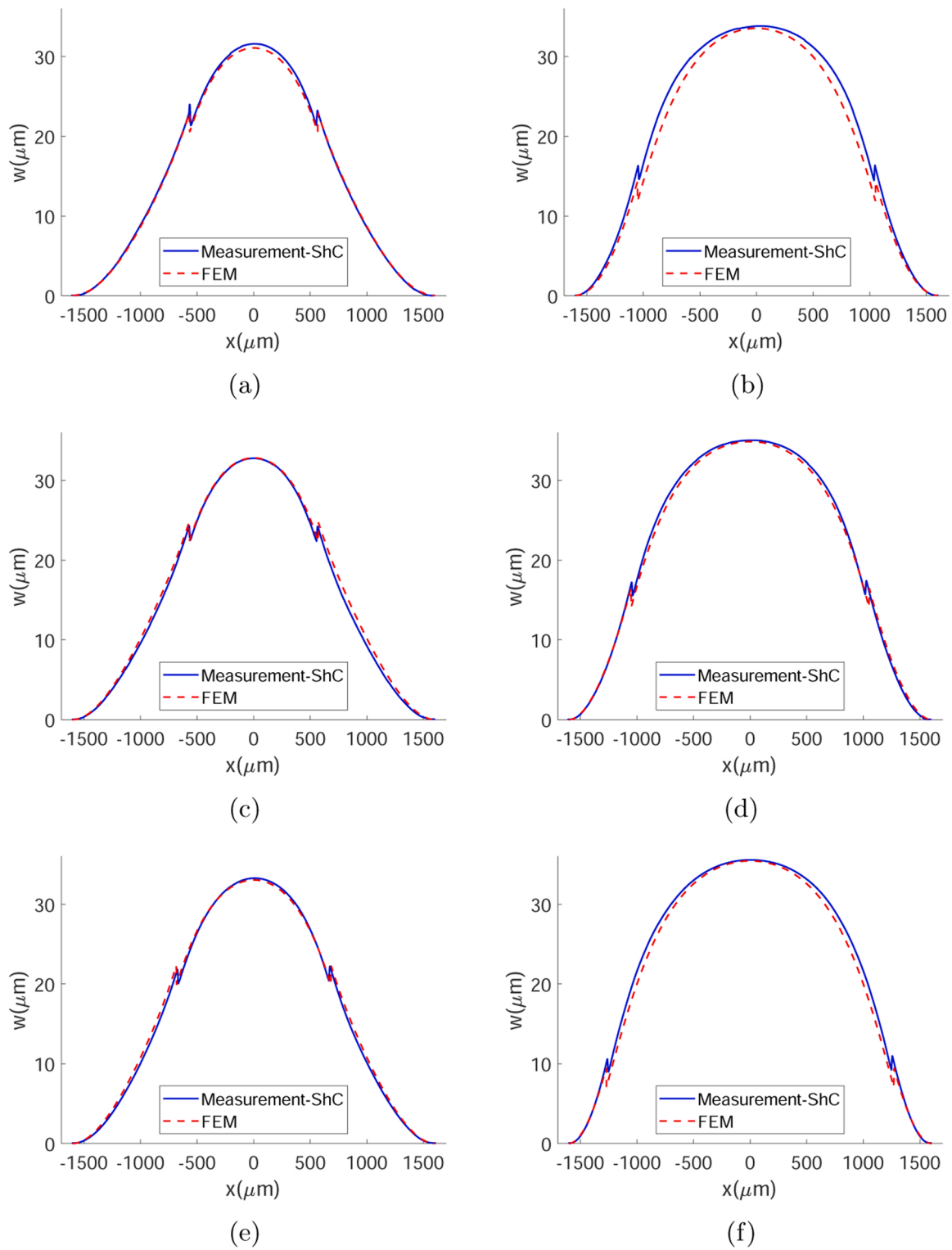
Fig. 5. Short-circuit (ShC) static deformation of the plates as a result of residual stress (a) CC1 (b) CC2 (C) SC1 (d) SC2 (e) SS1 (f) SS2.
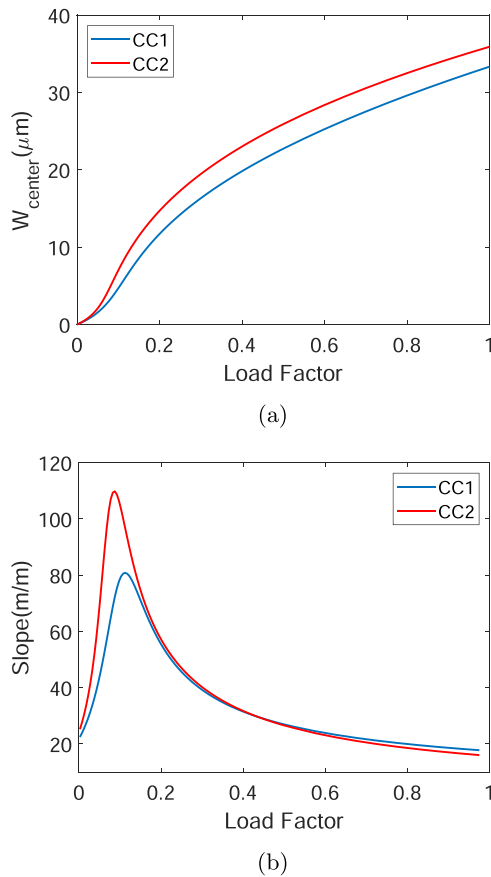
Fig. 6. Comparison of the (a) simulated center displacement of the CC1 and CC2 geometries by increasing the load factor and (b) their slope.
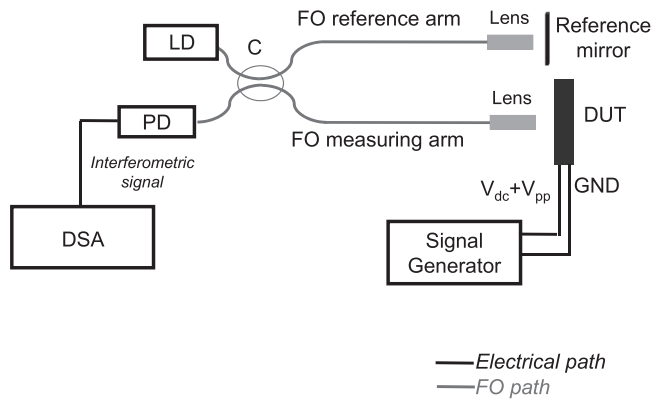

Fig. 7. Instrumental and optical configuration applied for characterizing piezo-actuated membranes (Device Under Test. DUT). LD: DFB Semiconductor Laser, $\lambda = 1550$ nm, PD: InGaAs Photodiode; C: 2×2, 50:50 fiberoptic coupler: FO: single-mode optical fiber; DSA: Dynamic Signal Analyzer.

detected by an InGaAs photodiode (FGA01FC Thorlabs, USA) (PD in Fig. 7) directly terminated on the 1 MΩ input resistance of a dynamic signal analyzer (DSA Agilent 35670A), that provides the frequency response by performing the Fast Fourier Transform (FFT) of the photo-detected signal. The sample under test is attached to a dedicated PCB, 30 mm x 43 mm. There are 3 connection ports on each PCB: the ground (GND) is connected to the lower electrode whereas the other ports are connected to the upper electrode and represent the electrical input for

the driving signal, which consists of a DC component V_{dc} plus a time-varying component with peak-to-peak amplitude V_{pp}, provided by a signal generator (KEYSIGHT 33500B). By applying a voltage, the piezo-electric actuator induces vibrations of the plate; a positive voltage between top and bottom electrodes induces upward bending of the plate. In particular, by driving the piezo-electric actuator with electrical white noise with $V_{pp} = 1$–3 V in the band 0 Hz - 130 kHz, it has been possible to excite several vibrational modes of the plate in the range 0 Hz - 100 kHz, that is the full span analyzed by the DSA.

As it is known from the theory of the laser interferometry, the photodetected interferometric signal V_{interf} follows the relationship:

$$V_{interf} \propto \cos[\phi_0 + 2k\Delta L(t)], \tag{1}$$

where ϕ_0 is the static phase difference between the electric field coming from the membrane and the electric field coming from the reference mirror, $k = 2\pi/\lambda$ is the wavenumber and $\Delta L(t)$ is the time-varying difference between the optical path of the interferometer arms due to the membrane displacement, along the direction of the impinging laser beam, induced by the electrically driven vibrations. Working in quadrature, that is for $\phi_0 = m(\pi/2)$, with m odd integer, the relationship becomes

$$V_{interf} \propto \sin[2k\Delta L(t)]. \tag{2}$$

For $\Delta L(t) < \lambda/20$, $V_{interf} \propto 2k\Delta L(t)$, in other words the interferometric signal is proportional to the vibration amplitude. If this condition is satisfied for the displacement amplitude of each excited vibration mode, the frequency response obtained by taking the FFT of the interferometric signal shows the amplitude resonance curves of the excited modes, centered at their resonance frequencies. Vibration measurements have been performed in the 5 positions of the membrane identified with the help of the red radiation emitted by a HeNe laser coupled into the fiberoptic path. These positions are indicated in Fig. 8. The frequency response has been acquired by shining the readout beam in different positions of the membrane since spatially resolved vibration measurements allow to identify the mode structure. As a matter of fact, not all the modes exhibit a detectable displacement in all the positions, since a position can be close to a vibration node (zero displacement) for a resonance mode. In these cases, the resonance curve associated to that mode is not present in the frequency response of the photodetected signal.

5. Results and discussion

As mentioned in the previous sections, we first confirm that both FE model and residual stress values are acceptable with static analysis. After that, the eigenvalue simulation is performed and the results are compared with dynamic measurement. A flowchart showing how the various simulation and measurement steps are connected is shown in Fig. 9.

Dynamic measurements were conducted on the aforementioned 5 points on the samples. The acquired frequency responses in positions 1 and 3 of the sample SC1 are shown in Fig. 10. The frequency response of the point 3 shows two peaks at the frequencies 37120 Hz and 43260 Hz, where no peak is observed in the frequency response measured at point 1. It means that the point 1 is close to a node of these two modes. Moreover, the resonances at 25340 Hz, 51970 Hz and 78340 Hz belong to centrosymmetric modes.

A comparison of the frequency response at all 5 points provides more information about the mode shape, and this is visualized in Figs. 11, 12, 13, 13, 14, 15, 16 which show FFT spectra of the interferometric signals collected in all positions and for three different values of V_{DC}. The resonance frequencies are marked by a label Ri, where i is an integer showing the mode number. These figures highlight which points are nodes for a mode at a specific resonance frequency. Although we could identify the resonance frequencies as well as the corresponding
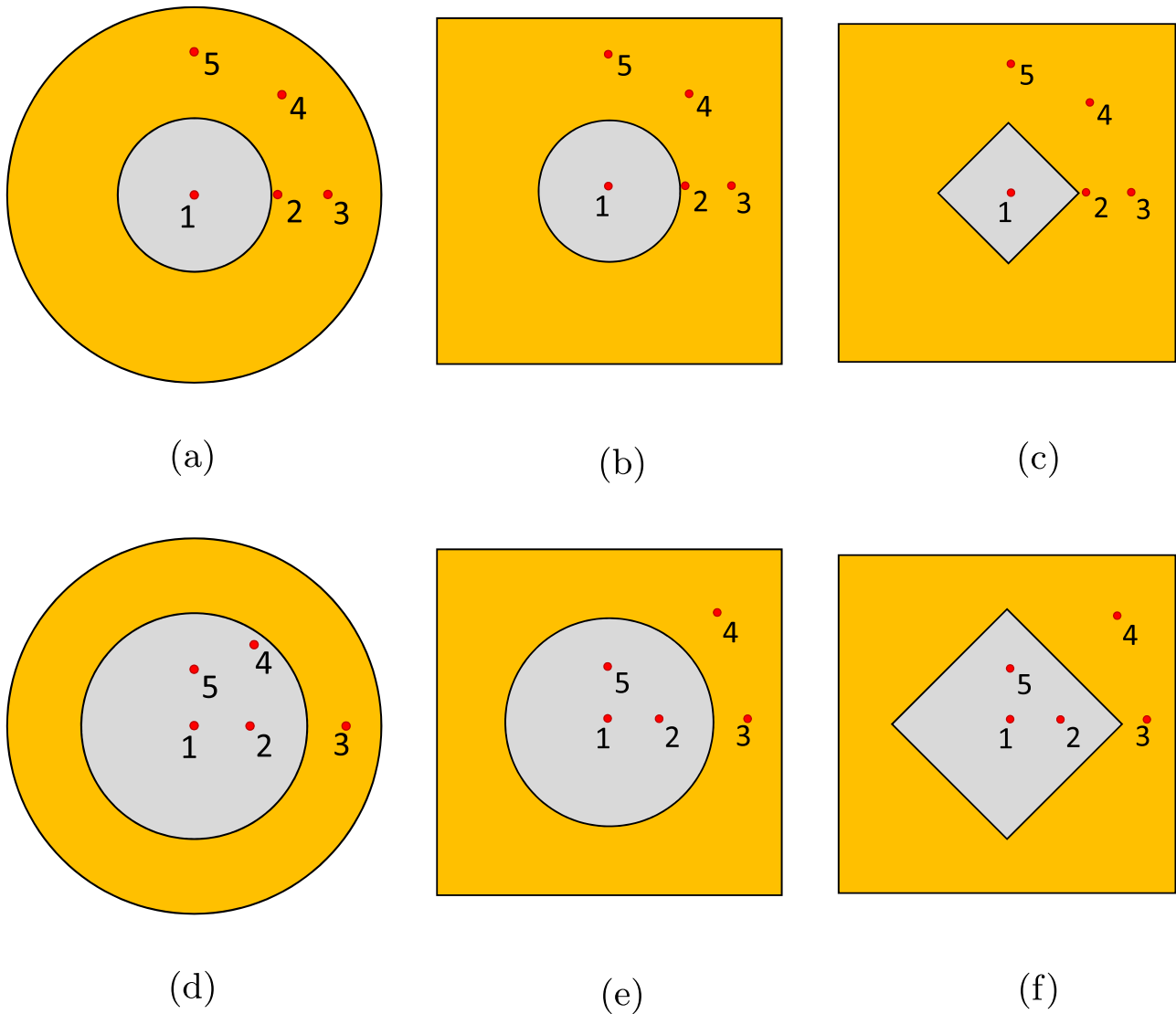
Fig. 8. Position of dynamic measurements on the plates to find the experimental resonance frequencies and mode shapes: (a) CC1, (b) SC1, (c) SS1, (d) CC2, (e) SC2, (f) SS2.

deformed and nodal points, it is still not sufficient to define the detailed mode shapes. Therefore, we utilize the FE simulation and match the measured deformed and nodal points with the mode shapes from FEM. The mode sequence is considered while matching mode shapes of both methods, unless two successive resonance frequencies are close to each other. The FE mode shapes and the comparison of the resonance frequencies from experiment and FEM are presented in Tabs. 6-11.

The resonance frequencies obtained numerically are in substantial agreement with the experimental values, although in some cases the difference can be up to 15%. The variablility in fabrication can be a source of error. For example in [36], sample-to-sample variations of about 9.78% in the resonance frequencies for buckled devices with the same configuration were reported.

For ideal samples and neglecting any material anisotropy, it is expected to observe only centrosymmetric mode shapes, because the geometry and actuating load have four-fold symmetry. However, as seen from Tabs. 6-11, some asymmetric modes are excited in experiments as well. The reason may be the existence of geometrical asymmetry in the fabricated samples as well as material anisotropy. Whereas all centrosymmetric modes are excited in all designs, in some samples, especially those with larger opening, fewer asymmetric modes are excited probably because in these cases the actuation load is lower than that present in samples with smaller opening. Therefore, the energy provided with the selected driving amplitude is not sufficiently high to induce a measurable displacement with our setup. On the other hand, applying a higher noise amplitude would induce a much larger displacement in more efficient modes, which could turn into a nonlinear behavior.

Comparing the resonance frequencies of the samples with the same configuration shows that the first resonance frequency of the larger opening is shifted more than that of the smaller opening due to the built-
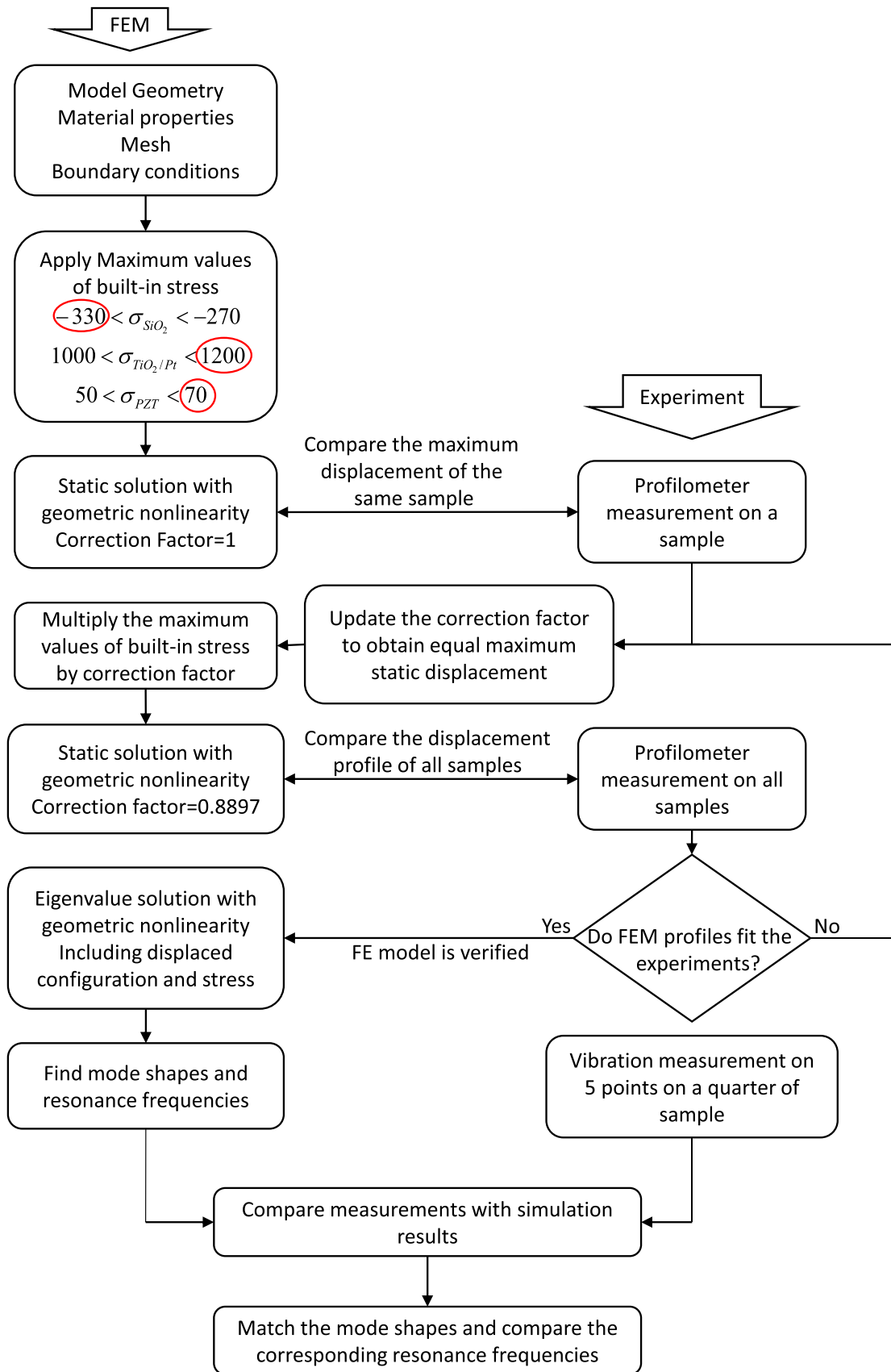
FEM

Model Geometry
Material properties
Mesh
Boundary conditions

Apply Maximum values
of built-in stress
$$-330 < \sigma_{SiO_2} < -270$$
$$1000 < \sigma_{TiO_2/Pt} < 1200$$
$$50 < \sigma_{PZT} < 70$$

Experiment

Static solution with
geometric nonlinearity
Correction Factor=1

Compare the maximum
displacement of the
same sample

Profilometer
measurement on a
sample

Multiply the maximum
values of built-in stress
by correction factor

Update the correction factor
to obtain equal maximum
static displacement

Static solution with
geometric nonlinearity
Correction factor=0.8897

Compare the displacement
profile of all samples

Profilometer
measurement on all
samples

Eigenvalue solution with
geometric nonlinearity
Including displaced
configuration and stress

Yes

FE model is verified

Do FEM profiles fit the
experiments?

No

Find mode shapes and
resonance frequencies

Vibration measurement on
5 points on a quarter of
sample

Compare measurements with simulation
results

Match the mode shapes and compare the
corresponding resonance frequencies

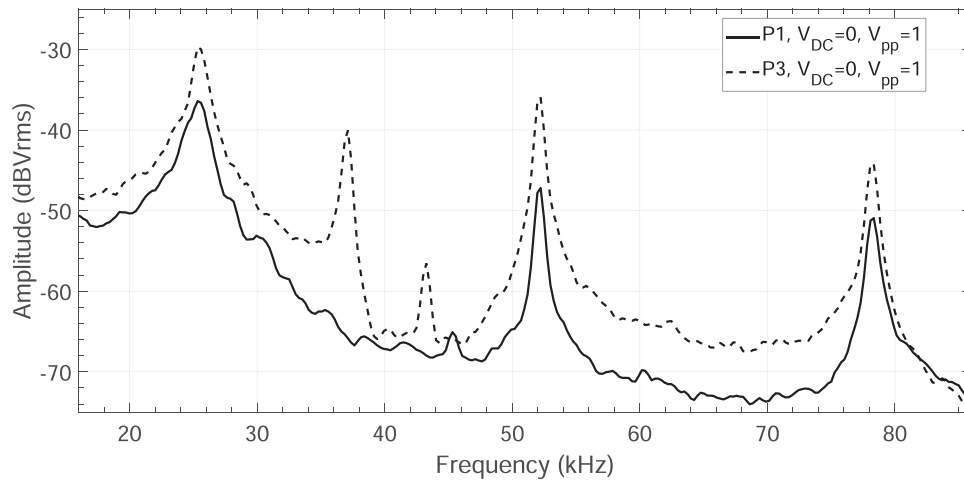**Fig. 9.** Simulation and measurement process flowchart.

Fig. 10. Measured frequency response of the photodetected signals on points 1 and 3 of the sample SC1.
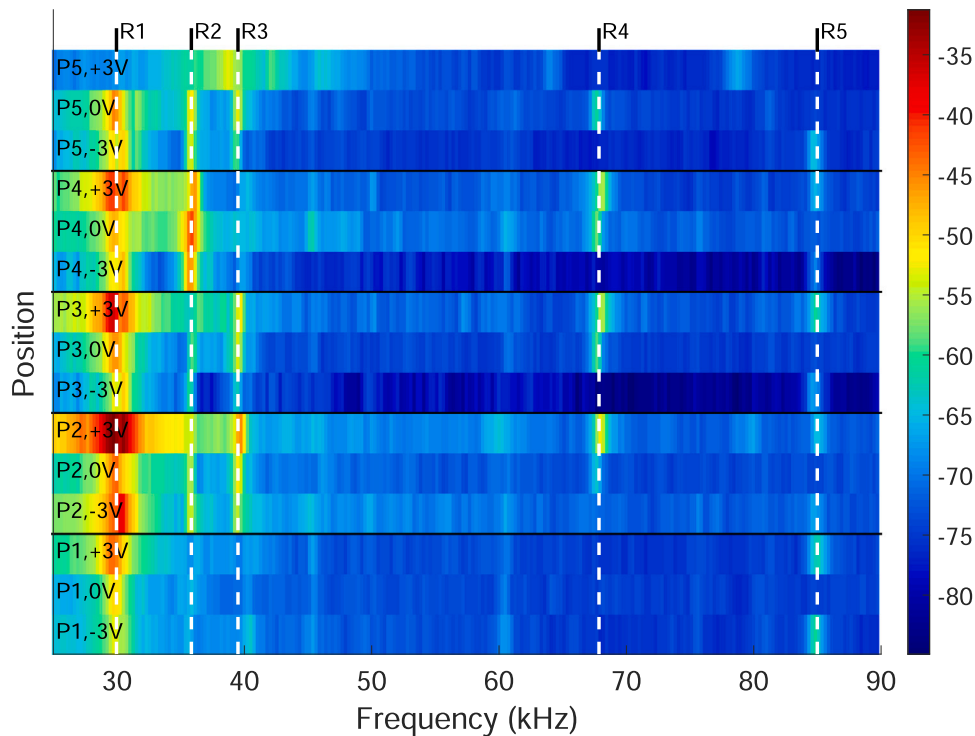

Fig. 11. Results of dynamic measurements of the plate CC1 in the frequency domain for the points P1-P5, and for $V_{pp} = 1$ V and $V_{DC} = -3$ V, 0 V and $+3$ V. Ri is the ith vibrating mode of the structure.

in stress. Our simulation shows that the first resonance frequencies of the sample CC1 and CC2 are 12990 Hz and 15087 Hz without built-in stress respectively, while they are respectively shifted up to 25335 Hz and 45555 Hz as the result of applying built-in stress. The reason of higher frequency shift of the sample CC2 can be the higher initial displacement as shown in Fig. 6, which induces more stiffening in-plane stresses. Therefore, its frequency is shifted more than the sample CC1. The same

behavior is observed in the other configurations.

A careful analysis of the results of the Figs. 11-16 shows that changing the bias voltage V_{DC} does affect the resonance frequency of some modes more than others. The same behavior is also predicted by FEM. For example, the frequency shift induced by changing the bias voltage is much larger for the modes 3, 4 and 6 of the sample CC2 than for the other modes. Both the measured and simulated resonance
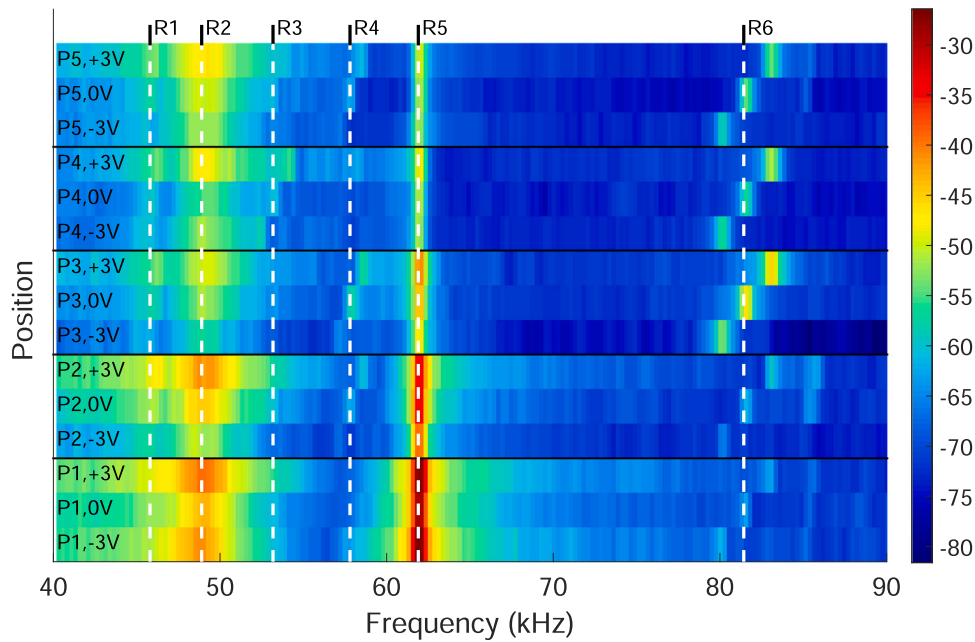
Fig. 12. Results of dynamic measurements of the plate CC2 in the frequency domain for the points P1-P5, and for $V_{pp} = 1$ V and $V_{DC} = -3$ V, 0 V and $+3$ V. Ri is the ith vibrating mode of the structure.
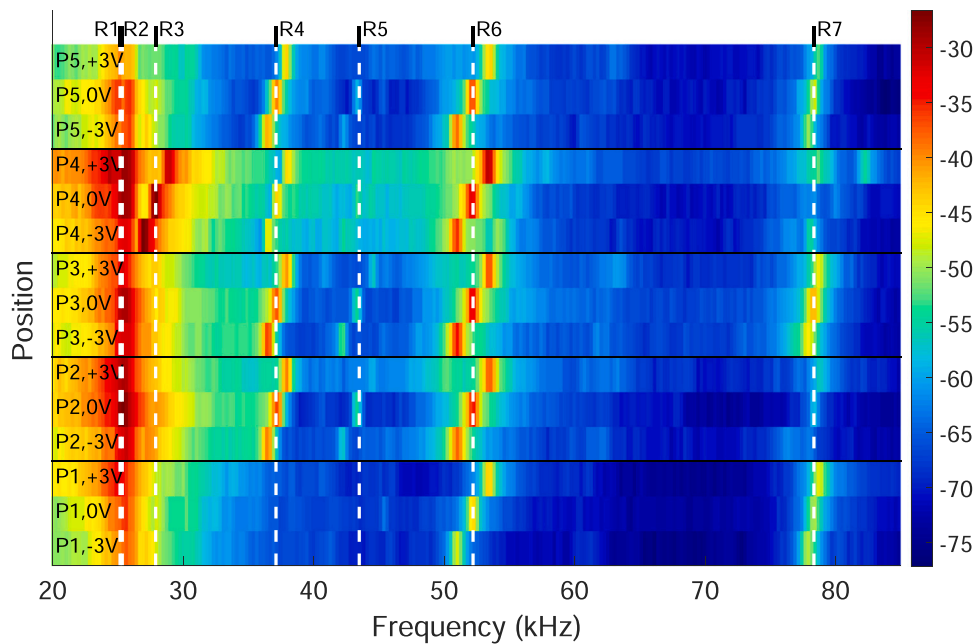

Fig. 13. Results of dynamic measurements of the plate SC1 in the frequency domain for the points P1-P5, and for $V_{pp} = 1$ V and $V_{DC} = -3$ V, 0 V and $+3$ V. Ri is the ith vibrating mode of the structure.

frequency for three different values of V_{DC} are presented in Tab. 12.

In Fig. 17, we report the frequency responses measured on sample CC2 on points 1 and 3 (also shown in Fig. 12), to better highlight the spectral lineshape variations induced by the different DC bias values, -3 V, 0 V and $+3$ V. When changing the DC voltage, the lineshape of the photodetected spectra are similar with the exception of the resonance frequency shift of the modes that are more strongly affected by the stiffness change. From this figure, we can conclude that the DC bias voltage is significant enough to shift the resonance frequency, but apart

from that the spectrum is qualitatively the same. In particular, we don't observe snap-through or jump phenomena.

The effect of the bias voltage on the resonance frequency of a buckled plate has been studied experimentally in [12], where the resonance frequency rate of change with bias voltage varies among the excited modes. It is also dependent on the buckled plate shape. The effect of the load factor on the resonance frequency shift induced by bias voltage has been calculated numerically, and the frequency shifts with respect to zero bias voltage are reported in Tab. 13, thus demonstrating that the
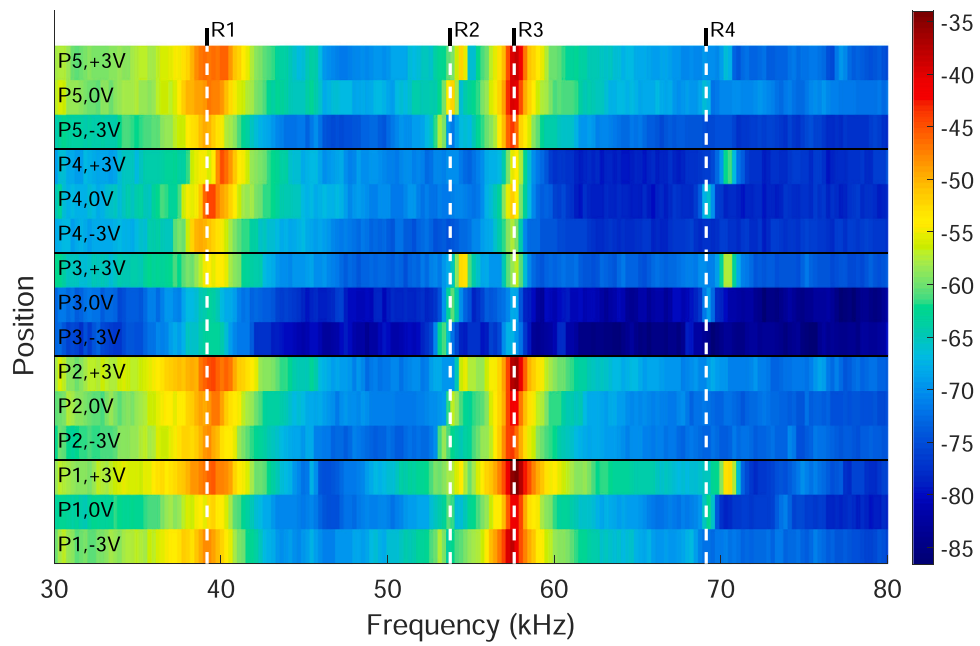
Fig. 14. Results of dynamic measurements of the plate SC2 in the frequency domain for the points P1-P5, and for $V_{pp} = 1$ V and $V_{DC} = -3$ V, 0 V and $+3$ V. Ri is the ith vibrating mode of the structure.
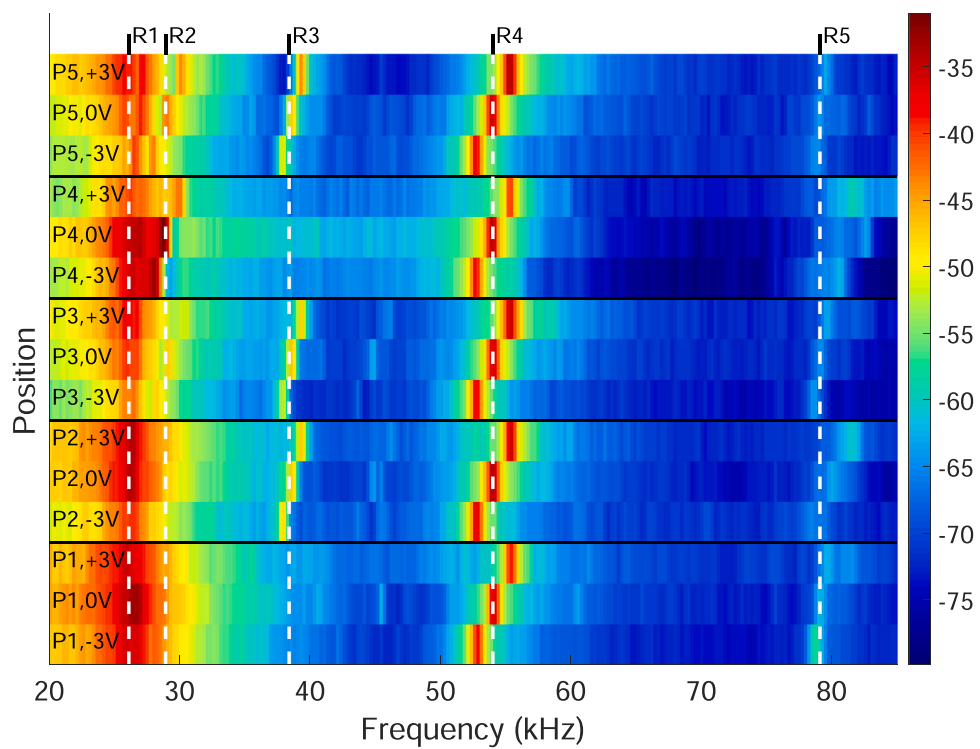

Fig. 15. Results of dynamic measurements of the plate SS1 in the frequency domain for the points P1-P5, and for $V_{pp} = 1$ V and $V_{DC} = -3$ V, 0 V and $+3$ V. Ri is the ith vibrating mode of the structure.

Table 6

Resonance frequencies and mode shapes of the plate CC1.

Resonance Mode shape	R1	R2	R3	R4	R5
FEM (Hz)	25335	34891	39696	66609	84972
Experiment (Hz)	29700	35580	39420	67330	84740
Difference (%)	14.7	1.9	0.7	1.1	0.3

Table 7

Resonance frequencies and mode shapes of the plate CC2.

Resonance Mode shape	R1	R2	R3	R4	R5	R6
FEM (Hz)	45555	45571	50359	54413	65868	82416
Experiment (Hz)	49150	45890	53180	57730	61820	81430
Difference (%)	7.3	0.7	5.3	5.7	6.5	1.2

Table 8

Resonance frequencies and mode shapes of the plate SC1.

Resonance Mode shape	R1	R2	R3	R4	R5	R6	R7
FEM (Hz)	21369	22856	24082	36847	39717	44945	78719
Experiment (Hz)	25340	25170	27900	37120	43260	51970	78340
Difference (%)	15.7	9.2	13.7	0.7	8.2	13.5	0.5

Table 9

Resonance frequencies and mode shapes of the plate SC2.

Resonance Mode shape	R1	R2	R3	R4
FEM (Hz)	34096	50502	57779	64789
Experiment (Hz)	38980	53630	57340	69120
Difference (%)	12.5	5.8	0.8	6.3

load factor affects the rate of change of the resonance frequency induced by bias voltage. For example, for a load factor of 0.5, the mode number 3 displays the largest rate of change by applying a bias voltage, while the largest resonance frequency change for a load factor equal to 1 occurs at the mode numbers 3 and 6.

The coercive field of the device limits us to apply a DC bias in the range of − 6 V to + 6 V. In order to investigate the behavior of the structure, the sample CC2 is simulated with DC bias beyond this limit,

where it is swept from − 20 V to + 20 V. This range is not applicable on the device as the polarization may switch at high voltages. In the simulation, it is assumed that the polarization direction is not changed, and we only study the structural behaviour. Fig. 18 shows the center point displacement for the geometric nonlinear static solution and the resonance frequencies of the device. It is observed that both resonance

Table 11

Resonance frequencies and mode shapes of the plate SS2.

Resonance Mode shape	R1	R2	R3	R4
FEM (Hz)	33633	35503	56967	70734
Experiment (Hz)	30460	41730	53500	81600
Difference (%)	10.4	14.9	6.5	13.3

Table 10

Resonance frequencies and mode shapes of the plate SS1.

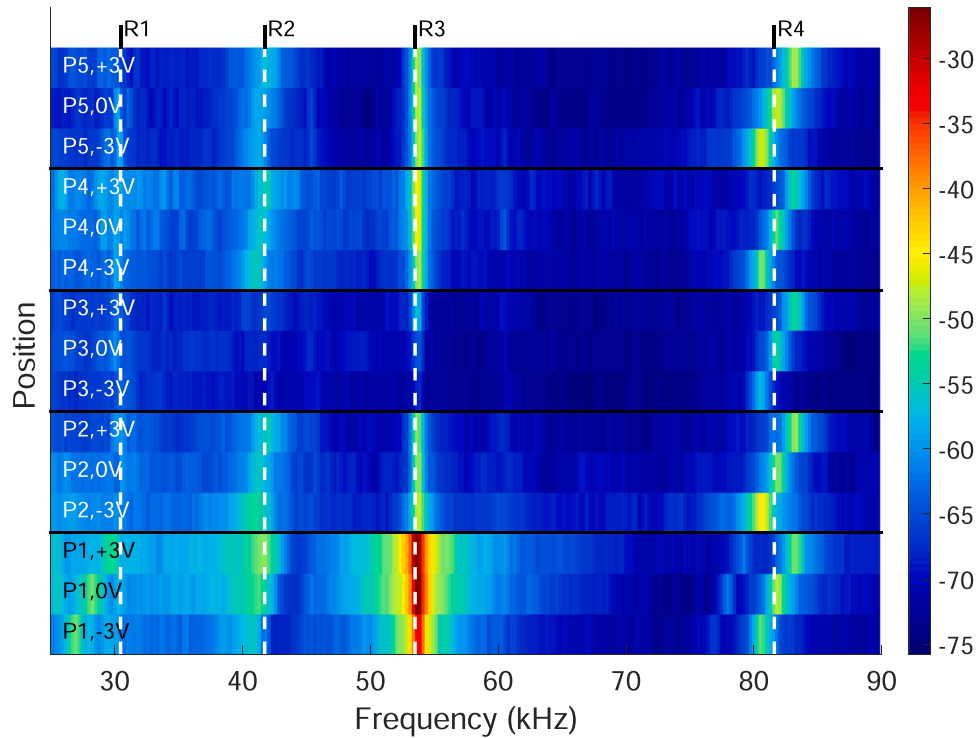| Resonance Mode shape	R1	R2	R3	R4	R5
FEM (Hz)	21998	23791	38559	47871	80060
Experiment (Hz)	25860	28930	38400	54020	79100
Difference (%)	14.9	17.8	0.4	11.4	1.2

Fig. 16. Results of dynamic measurements of the plate SS2 in the frequency domain for the points P1-P5, and for $V_{pp} = 1$ V and $V_{DC} = -3$ V, 0 V and $+3$ V.

Table 12
Effect of bias voltage on the resonance frequency of the plate CC2, and a comparison between the simulation with Load Factor= 1 and experiment.

	Resonance frequency with bias voltage (Hz)		
	Mode Nr.	+ 3 V	0 V	-3 V
Comsol	1	45920	45555	45155
Experiment	1	49280	49150	48900
Comsol	2	46361	45571	44764
Experiment	2	46340	45890	45500
Comsol	3	52245	50359	48410
Experiment	3	54140	53180	52350
Comsol	4	56046	54413	52741
Experiment	4	58430	57730	57020
Comsol	5	65282	65865	66555
Experiment	5	61820	61820	61760
Comsol	6	85507	82416	79226
Experiment	6	82970	81430	79960

frequencies and center point displacements are changed linearly by changing the DC bias voltage within the applicable voltage range. It can be concluded that the the behavior of the structure is a linear function of the bias voltage near the initially deformed configuration, as the piezoelectric stress induced by the DC bias voltage is not high compared with the built-in stress.

A negative DC bias will stretch the PZT layer, which results in a compressive load on the internal zone, which is not covered with PZT. In addition, a bending moment is applied on the device as a result of PZT actuation. The schematic of the force and moment is shown in Fig. 19. Therefore, the compressive load will force the center point displacement to increase, and resonance frequencies decrease. Interestingly, a snap-through behavior occurs at around -16 V DC bias, where the upward buckled plate switches to the downward buckled configuration. The reason of this behavior is the bending moment of actuation, which rises to a point to move the plate to the second stability position.
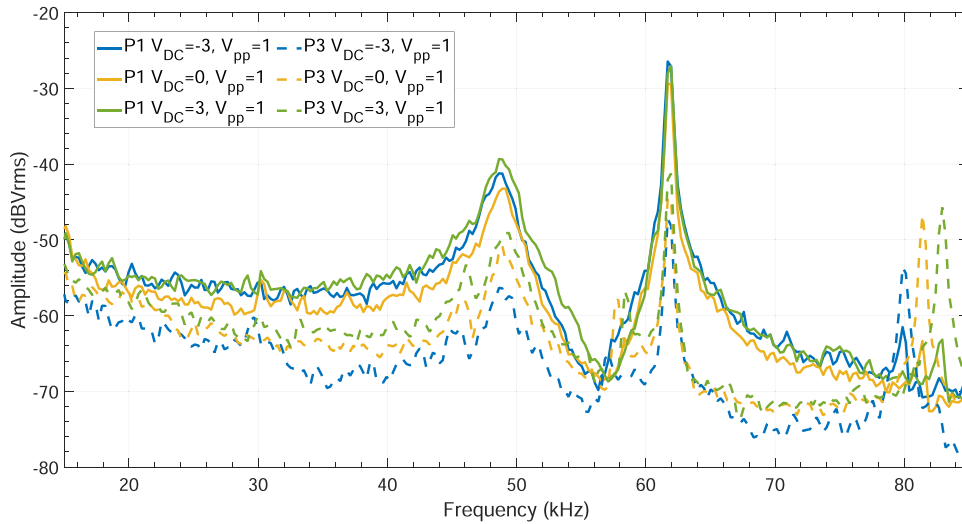
Fig. 17. Measured frequency response of the photodetected signals on points 1 and 3 of the sample CC2 for + 3 V, 0 V and − 3 V DC bias.

Table 13
Effect of bias voltage and load factor on the resonance frequency of the plate CC2.

| | Difference in resonance frequency from that of 0-V bias (%) | | | |
| | Load Factor= 0.5 | | Load Factor = 1 | |
Mode Nr.	+ 3 V	-3 V	+ 3 V	-3 V
1	1.71	-1.90	0.80	-0.88
2	2.37	-2.50	1.73	-1.77
3	3.52	-3.69	3.74	-3.87
4	2.80	-2.90	3.00	-3.07
5	-0.71	0.84	-0.88	1.05
6	2.28	-2.35	3.75	-3.87

Although this simulation is unrealistic as the − 16 V bias voltage will change the polarization of the piezoelectric layer, it may happen if the device is fabricated with lower built-in stress. For example, if we divide the built-in stress by 4, which means the load factor equals 0.25, the snap-through voltage will drop to − 3.6 V. This voltage is within the applicable range of the piezoelectric layer, which means that this behavior may happen in a buckled plate.

6. Conclusion

In this paper, a simple interferometric setup realized with a diode laser, a fiberoptic coupler, two lenses and a photodiode has been employed to characterize the dynamic frequency response of initially deformed piezo-actuated plates. The static displacement by equi-biaxial built-in stresses of different layers is fed to a geometrically nonlinear FE model and numerical results are compared with experimental profilometric measurement. The good agreement in the values of static displacement validates the FE model. The FE model is then utilized to match the mode shapes with the interferometric experimental results. In comparison with a conventional LDV instrument, vibration measurements were performed just in a limited number of positions. Then, we can match the frequency response profile and resonance frequency values with the mode shapes from FEM. Numerical and experimental results are in good agreement, which demonstrates the capability of FEM for an accurate simulation of the device dynamic behavior. Therefore, our combination of FEM and spot optical measurements in a discrete number of positions is capable of matching resonance frequencies and mode shapes of an initially deformed micro-plate. By studying the effect
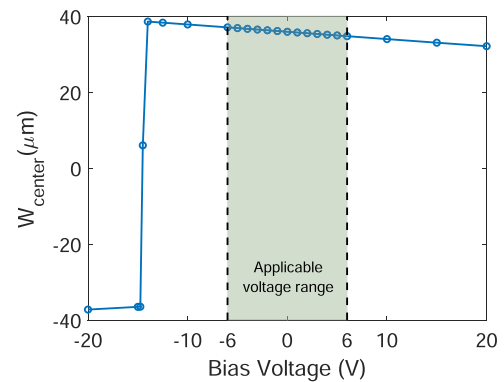
(a)
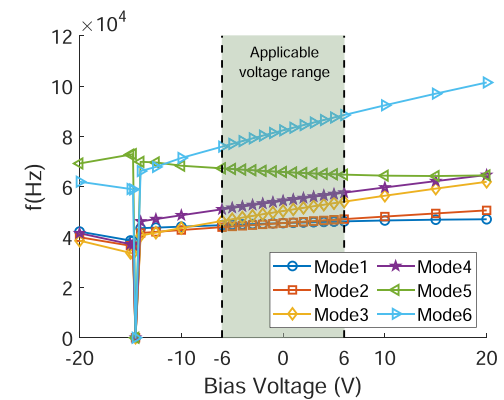
(b)

Fig. 18. Effect of DC bias on (a) the center displacement and (b) resonance frequencies of the sample CC2.
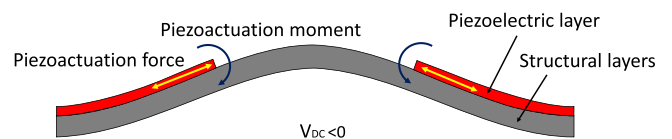

Fig. 19. Force and bending moment applied by PZT actuation.

of bias voltage on the resonance frequency, we have observed both numerically and experimentally that some modes are affected more than others by the bias voltage. The frequency shift induced by bias voltage is also dependent on the amount of built-in stress. Furthermore, a bias voltage may change the stability position of a buckled plate via snap-through phenomena.

CRediT authorship contribution statement

Hamed Salmani: Conceptualization, Methodology, Software, Validation, Formal analysis, Investigation, Resources, Data curation, Writing-original draft, Visualization. Elisabetta Bodo: Formal analysis, Investigation, Data curation, Visualization. Ulrik Hanke: Conceptualization, Methodology, Writing - review and editing, Supervision, Funding acquisition. Andreas Vogl: Methodology, Investigation, Validation, Writing - original draft. Shruti Jain: Methodology, Validation, Investigation, Writing - original draft, Project administration. Sabina Merlo: Conceptualization, Methodology, Investigation, Resources, Writing - review and editing, Supervision. Einar Halvorsen: Conceptualization, Methodology, Writing - review and editing, Supervision, Project administration, Funding acquisition.

Declaration of Competing Interest

The authors declare the following financial interests/personal relationships which may be considered as potential competing interests: Einar Halvorsen reports financial support was provided by Research Council of Norway. Einar Halvorsen reports a relationship with Polight AS that includes: non-financial support.

Acknowledgement

References

[1] M.A. Farghaly, U. Hanke, M.N. Akram, E. Halvorsen, Trial functions for reduced-order models of piezoelectrically actuated microelectromechanical systems tunable lenses, Opt. Eng. 57 (09) (2018) https://doi.org/10.1117/1.OE.57.9.095103.

[2] S. Merlo, E. Crisa, M. Ferrera, M. Soldo, Experimental Detection of Piezo-Tunable Micro-Lens Performances by Spot Optical Measurements, in:2019 20th International Conference on Solid-State Sensors, Actuators and Microsystems & Eurosensors XXXIII (TRANSDUCERS & EUROSENSORS XXXIII), IEEE, 2019, 1541–1544.

[3] S. Merlo, E. Crisà, D. Giusti, M. Ferrera, M. Soldo, Characterization of Tunable Micro-Lenses with a Versatile Optical Measuring System, Sensors 18 (12) (2018) 4396, https://doi.org/10.3390/s18124396.

[4] F. Akasheh, T. Myers, J.D. Fraser, S. Bose, A. Bandyopadhyay, Development of piezoelectric micromachined ultrasonic transducers, Sensors and Actuators A: Physical 111 (2–3)(2004)275–287.10.1016/j.sna.2003.11.022.

[5] L. Medina, R. Gilat, S. Krylov, Bistable behavior of electrostatically actuated initially curved micro plate, Sens. Actuators A: Phys. 248 (2016) 193–198, https://doi.org/10.1016/j.sna.2016.07.027.

[6] K. Yamashita, H. Tanaka, M. Noda, Highly sensitive structures for ultrasonic microsensors by buckling control of diaphragms through intrinsic stress of PZT films, in: IEEE SENSORS 2014 Proceedings, Vol. 2014-Decem, IEEE, 2014, pp. 106–109.10.1109/ICSENS.2014.6984944.⟨https://ieeexplore.ieee.org/document/6984944⟩.

[7] A. Biswas, T. Weller, L.P.B. Katehi, Stress determination of micromembranes using laser vibrometry, Rev. Sci. Instrum. 67 (5) (1996) 1965–1969, https://doi.org/10.1063/1.1146952.

[8] M. Olfatnia, T. Xu, L.S. Ong, J.M. Miao, Z.H. Wang, Investigation of residual stress and its effects on the vibrational characteristics of piezoelectric-based multilayered microdiaphragms, J. Micromech. Microeng. 20 (1) (2010), 015007, https://doi.org/10.1088/0960-1317/20/1/015007.

[9] C.-C. Lee, G. Cao, I. Shen, Effects of residual stresses on lead-zirconate-titanate (PZT) thin-film membrane microactuators, Sens. Actuators A: Phys. 159 (1) (2010) 88–95, https://doi.org/10.1016/j.sna.2010.02.022.

[10] K. Yamashita, K. Tomiyama, K. Yoshikawa, M. Noda, M. Okuyama, Resonant frequency tuning of piezoelectric ultrasonic microsensors by bias voltage application to extra top-electrodes on PZT diaphragms, Ferroelectrics 408 (1) (2010) 48–54, https://doi.org/10.1080/00150193.2010.485014.

[11] K. Yamashita, T. Nishioka, M. Noda, P. Muralt, Vibration Mode Investigation of Piezoelectric Ultrasonic Microsensors on Buckled Diaphragms, Proceedings 2 (13) (2018) 835, https://doi.org/10.3390/proceedings2130835.

[12] K. Yamashita, H. Hibino, T. Nishioka, M. Noda, P. Muralt, Vibration Mode of MEMS Ultrasonic Sensors on Buckled Diaphragms with Piezoelectric Resonance Frequency Modification, Proc. IEEE Sens. 2019-Octob (2019) 3–6, https://doi.org/10.1109/SENSORS43011.2019.8956622.

[13] T. Nishiumi, K. Yamashita, H. Tanaka, K. Arai, M. Noda, Vibration mode analysis on piezoelectric diaphragms for ultrasonic microsensors,in:2015 IEEE International Meeting for Future of Electron Devices, Kansai (IMFEDK), IEEE, 2015, 86–87.10.1109/IMFEDK.2015.7158562.

[14] K. Yamashita, T. Nishioka, T. Nishiumi, M. Noda, Influence of top electrodes to vibration modes in impulse responses of MEMS piezoelectric diaphragms for ultrasonic microsensors, Procedia Eng. 168 (2016) 844–847, https://doi.org/10.1016/j.proeng.2016.11.287.

[15] J.B. Messaoud, J.F. Michaud, D. Certon, M. Camarda, N. Piluso, L. Colin, F. Barcella, D. Alquier, Investigation of the youngas modulus and the residual stress of 4H-SiC Circular membranes on 4H-SiC substrates, Micromachines 10 (12) (2019) 1–12, https://doi.org/10.3390/mi10120801.

[16] M. Dorfmeister, M. Schneider, U. Schmid, 3D characterisation of piezoelectric bistable MEMS membranes during switching, Sens. Actuators, A: Phys. 298 (2019), 111576, https://doi.org/10.1016/j.sna.2019.111576.

[17] S. Merlo, P. Poma, E. Crisà, D. Faralli, M. Soldo, Testing of Piezo-Actuated Glass Micro-Membranes by Optical Low-Coherence Reflectometry, Sensors 17 (3) (2017) 462, https://doi.org/10.3390/s17030462.

[18] G. Viola, J. Chang, T. Maltby, F. Steckler, M. Jomaa, J. Sun, J. Edusei, D. Zhang, A. Vilches, S. Gao, X. Liu, S. Saeed, H. Zabalawi, J. Gale, W. Song, Bioinspired Multiresonant Acoustic Devices Based on Electrospun Piezoelectric Polymeric Nanofibers, ACS Appl. Mater. Interfaces 12 (31) (2020) 34643–34657, https://doi.org/10.1021/acsami.0c09238.

[19] V. Annovazzi-Lodi, M. Benedetti, S. Merlo, M. Norgia, Optical Detection of Multiple Modes on Resonant Micromachined Structures, IEEE Photonics Technol. Lett. 16 (7) (2004) 1703–1705, https://doi.org/10.1109/LPT.2004.828841.

[20] G. Silva, F. Carpignano, F. Guerinoni, S. Costantini, M. De Fazio, S. Merlo, Optical Detection of the Electromechanical Response of MEMS Micromirrors Designed for Scanning Picoprojectors, IEEE J. Sel. Top. Quantum Electron. 21 (4) (2015) 147–156, https://doi.org/10.1109/JSTQE.2014.2369499.

[21] Y.-C. Wu, Y.-H. Huang, C.-C. Ma, Theoretical analysis and experimental measurement of flexural vibration and dynamic characteristics for piezoelectric rectangular plate, Sens. Actuators A: Phys. 264 (2017) 308–332, https://doi.org/10.1016/j.sna.2017.07.034.

[22] Q. He, G. Zhang, C. Zheng, K. Chen, W. Zhao, L. Qiu, Laser confocal vibration measurement method with high dynamic range, Opt. Express 28 (7) (2020) 9965, https://doi.org/10.1364/OE.387933.

[23] Y. Zhang, T. Hiruta, I. Kajiwara, N. Hosoya, Active vibration suppression of membrane structures and evaluation with a non-contact laser excitation vibration test, J. Vib. Control 23 (10) (2017) 1681–1692, https://doi.org/10.1177/1077546315599302.

[24] M. Hadipour, M. Tahtali, A. Lambert, Design and characterization of a vibrating piezo-membrane deformable mirror for adaptive optics application, in: K.U. Stein, S. Gladysz (Eds.), Environmental Effects on Light Propagation and Adaptive Systems, SPIE, 2018, p. 12, https://doi.org/10.1117/12.2326527.

[25] H. Jia, M.H. Matheny, M.L. Roukes, P.X.-L. Feng, Multimode Vibrations in High-Frequency Aluminum Nitride Piezoelectric Nanomembrane Resonators, in:2019 20th International Conference on Solid-State Sensors, Actuators and Microsystems & Eurosensors XXXIII (TRANSDUCERS & EUROSENSORS XXXIII), no. June, IEEE, 2019, 442–445.10.1109/TRANSDUCERS.2019.8808643.

[26] T. Bakke, A. Vogl, O. Zero, F. Tyholdt, I.R. Johansen, D. Wang, A novel ultra-planar, long-stroke and low-voltage piezoelectric micromirror, J. Micromech. Microeng. 20 (6) (2010), https://doi.org/10.1088/0960-1317/20/6/064010.

[27] H. Ræder, F. Tyholdt, W. Booij, F. Calame, N.P. Østbø, R. Bredesen, K. Prume, G. Rijnders, P. Muralt, Taking piezoelectric microsystems from the laboratory to production, J. Electroceram. 19 (4) (2007) 357–362, https://doi.org/10.1007/s10832-007-9036-3.

[28] G. Janssen, M. Abdalla, F. van Keulen, B. Pujada, B. van Venrooy, Celebrating the 100th anniversary of the Stoney equation for film stress: Developments from polycrystalline steel strips to single crystal silicon wafers, Thin Solid Films 517 (2009) 1858–1867, https://doi.org/10.1016/j.tsf.2008.07.014.

[29] M.A. Hopcroft, W.D. Nix, T.W. Kenny, What is the Young's Modulus of Silicon? J. Micro Syst. 19 (2010) 229–238, https://doi.org/10.1109/JMEMS.2009.2039697.

[30] V. Chivukula, M. Wang, H.F. Ji, A. Khaliq, J. Fang, K. Varahramyan, Simulation of SiO 2-based piezoresistive microcantilevers, Sens. Actuators, A: Phys. 125 (2) (2006) 526–533, https://doi.org/10.1016/j.sna.2005.08.038.

[31] W.J. Yoon, P.G. Reinhall, E.J. Seibel, Analysis of electro-active polymer bending: A component in a low cost ultrathin scanning endoscope, Sens. Actuators, A: Phys. 133 (2 SPEC. ISS.) (2007) 506–517, https://doi.org/10.1016/j.sna.2006.04.037.

[32] C.-W. Baek, Y.-K. Kim, Y. Ahn, Y.-H. Kim, Measurement of the mechanical properties of electroplated gold thin films using micromachined beam structures, Sens. Actuators A: Phys. 117 (1) (2005) 17–27, https://doi.org/10.1016/j.sna.2003.11.041.

[33] M.A. Farghaly, M.N. Akram, E. Halvorsen, Modeling framework for piezoelectrically actuated MEMS tunable lenses, Opt. Express 24 (25) (2016) 28889, https://doi.org/10.1364/oe.24.028889.

[34] M.A. Farghaly, M.N. Akram, E. Halvorsen, Optical performance of piezoelectrically actuated MEMS tunable lenses with various pupil geometries, Opt. Eng. 56 (3) (2017), 035104, https://doi.org/10.1117/1.oe.56.3.035104.

[35] COMSOL Multiphysics v. 5.5.⟨www.comsol.com⟩, COMSOL AB, Stockholm, Sweden.

[36] K. Yamashita, T. Nishiumi, H. Tanaka, M. Noda, Vibration modes in impulse response of piezoelectric diaphragms for ultrasonic microsensors, in: 2016 IEEE 11th Annual International Conference on Nano/Micro Engineered and Molecular Systems (NEMS), 2016, 300–304.10.1109/NEMS.2016.7758254.

Ulrik Hanke (IEEE SM'06) received the Siv.Ing. and the Dr.Ing. degrees in physics from the Norwegian University of Science and Technology (NTNU), Trondheim, Norway, in 1989 and 1994, respectively. After two years as a Post. Doc. he worked for a decade as a research scientist at department of communication technology, SINTEF. Since 2006, he has been with University of South-Eastern Norway, Borre, where he is a Professor of Micro- and Nanosystem technology. His current main research interests are in theory, design, and modelling of piezoelectric and RF acoustic micro devices.

Hamed Salmani received his PhD in aerospace engineering from Tarbiat Modares University, Iran, in 2018 and MSc in aerospace engineering from Sharif University of Technology, Iran, in 2011. He continued his research in piezoelectric actuators at University of South-Eastern Norway (USN) as a postdoctoral research fellow from 2019 to 2021. Since March 2021, he has been working as an associate professor at USN. His main research areas are analytical and numerical modelling and characterization of piezoelectric devices including actuator, energy harvester, ultrasonic transducer, and RF acoustic filters.

Sabina Merlo received the PhD degree in electronic engineering from University of Pavia (UNIPV), Italy, in 1991 and the MSE. degree in bioengineering from UW, Seattle, in 1989. She was recipient of a Rotary Foundation Graduate Scholarship for study at UW. Associate Professor since 2001 at UNIPV, she is since 2018 Full Professor of Electronic measurements at the Department of Electrical, Computer and Biomedical Engineering, UNIPV. Her research interests include optical measurements on MEMS, MOEMS and microfluidic devices, optical interferometry, fiberoptic components and sensors. She holds 4 patents and is coauthor of 200 publications in journals, books, and conference proceedings.

Elisabetta Bodo was born in Novara, Italy, in 1996. She received the bachelor's degree in bioengineering and the master's degree in electronic engineering from the University of Pavia in 2018 and 2020, respectively. Her MSc thesis was focused on the development of a smart micro-opto-fluidic platform for analytical detection of fluids. She is currently a Ph.D. student at the University of Pavia, working on the characterization of micro-opto-electro-mechanical systems (MOEMS). Her research interests include photonics and optoelectronics for the development of micro-sensors.

Andreas Vogl completed his Dipl. Ing. in electrical engineering at the University of Erlangen-Nuremberg, Germany, in 2002. His diploma thesis was entitled Nanocrystals for non-volatile memories. He works at the Microsystems department of SINTEF as a senior scientist for MEMS-design. His research interests are modelling and simulation (both finiteelement and on a system level), process integration of microsystems, piezoMEMS and nanotechnology for MEMS. He has authored and co-authored more than 50 journal articles and conference papers and one book chapter. He also holds several patents.

Shruti Jain completed her M.Tech. in Materials Science at Indian Institute of Technology, Mumbai, India. Her thesis was on the topic "Continuous synthesis of YSZ nanoparticles" and is an important part of the SINTEF MEMS team. She works as Master of Science at SINTEF MiNaLab and is experienced in Process development, Micro and Nano film depositions and front-end fabrication. She has a broad understanding of engineering lab processes and has been involved in processing for PiezoMEMS group and BCB bonding at SINTEF.

Einar Halvorsen received the Siv.Ing. degree in physical electronics from the Norwegian Institute of Technology (NTH), Trondheim, Norway, in 1991, and the Dr.Ing. degree in theoretical solid state physics from the Norwegian University of Science and Technology (NTNU, formerly NTH), Trondheim, Norway, in 1996. After a postdoc position at the University of Oslo and five years in industry, he joined Vestfold University College, now University of South-Eastern Norway, in Horten, Norway where he is a professor of micro and nanotechnology. His main research interest is in theory, design, and modeling of microelectromechanical devices. Much of his recent research has focused on MEMS vibration energy harvesting or piezoelectric actuators.